




Problems Associated with Making Mechanical Measurements on Water–Ice at Quasistatic and Dynamic Strain Rates

Ryan S. Potter¹  · Joseph M. Cammack¹ · Christopher H. Braithwaite¹ · Philip D. Church² · Stephen M. Walley¹

Received: 28 March 2019 / Accepted: 11 June 2019
© The Author(s) 2019

Abstract

Space penetrators are a potential method of inserting instrumentation onto ice-covered bodies in the solar system. Part of a study to see whether this is feasible involves numerically simulating impact of the penetrator into ice at impact velocities of a few 100 m/s. In order to do this accurately, it is necessary to have a constitutive model for water ice that is valid at the strain rates and temperatures relevant to impact in the Outer Solar System. This paper reports certain issues and difficulties that arose during a study to obtain this data.

Introduction

Space penetrators have been suggested as a cost-effective method of placing instrumentation on an icy body in the Outer Solar System such as Europa [1–3]. Such probes would also be lighter and mechanically simpler than reverse-thruster landers and produce much less contamination of the surface it is desired to study [4].

Although there have been a number of published studies on hypervelocity impact and shock studies of ice [5–11] performed so as to understand what happens in the Solar System on a regular basis without human involvement, ballistic impact on ice targets at more modest impact velocities (100 m/s) has been comparatively little studied [12–18]. In order to design a space probe capable of surviving impact on Europa, it is necessary to know the mechanical properties of water–ice at the appropriate strain rate and temperature. This investigation was therefore performed in order to build upon the existing body of literature on water ice at high strain rates (Fig. 1, 2, 3) [19–26].

Water ice is a material with a wide range of properties [30, 31]. Indeed, Carney et al. say it should be regarded as a class of materials rather than as one specific material [19]. At the fundamental level, pure water ice exists in seventeen

known crystalline forms [31] (Fig. 4). In the world outside the laboratory, the way a body of ice forms introduces many other complications such as solutes [32, 33], gases [34, 35] and solid matter (dirt) [36–38]. Such contaminants are known to have an effect on the compressive strength of ice [39–43].

Intrinsic factors that need to be considered when preparing ice specimens for mechanical testing include porosity, salinity, temperature, grain size and orientation. Extrinsic factors include rate of loading, confinement conditions, direction of loading relative to crystallographic axis, sample size and preparation method. In this study we restricted ourselves to investigating pure water ice on the grounds that it is the easiest form of ice to make chemically and mechanically reproducible specimens from. Also if a probe can be designed to withstand impact on pure ice, it is likely to be able to survive impact on the damaged and impure ice that likely exists on the surface of Europa.

Optical measurements of the surface temperature of Europa give values between 86 and 132 K, depending on the latitude and time of day [44, 45]. The atmospheric surface pressure is believed to be $\approx 1 \times 10^{-6}$ Pa [46, 47]. Thus the stable phase of ice would be I, which exists in both hexagonal (Ih) and cubic (Ic) forms.

In order to obtain mechanical data on the right sort of ice, it is necessary to give some thought as to what state the uppermost few metres of ice on Europa is likely to be in [48]. It has been suggested that, due to amorphization caused by radiation (and other processes), amorphous ice will continuously form on the upper surface, which will then slowly crystallize to ice Ic at temperatures typical

✉ Stephen M. Walley
smw14@cam.ac.uk

¹ SMF Fracture and Shock Physics Group, The Cavendish Laboratory, J.J. Thomson Avenue, Cambridge CB3 0HE, UK

² QinetiQ Fort Halstead, Sevenoaks, Kent TN14 7BP, UK

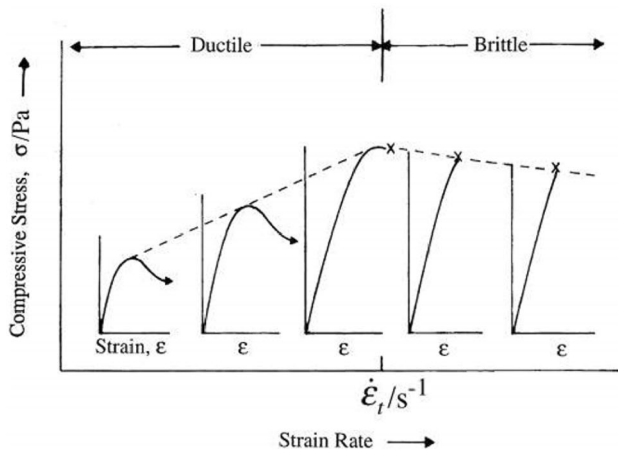


Fig. 1 Schematic diagram of the effect of strain rate on the compressive stress–strain curve for water ice. From [27]

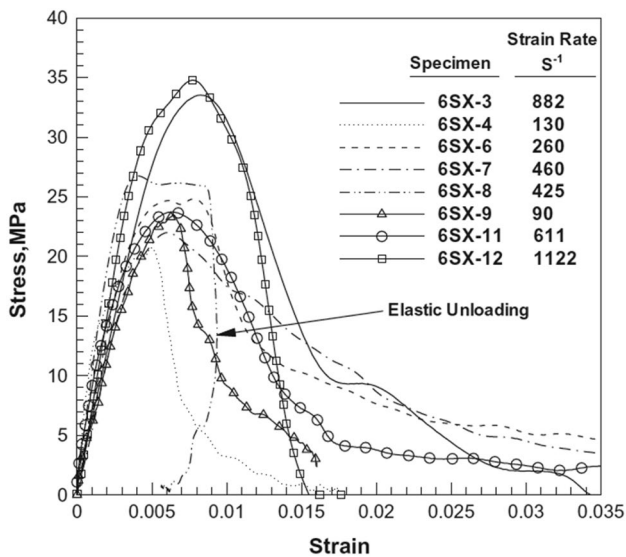


Fig. 2 High rate stress–strain curves for single crystal ice at $-10\text{ }^{\circ}\text{C}$ obtained using an SHPB. From [21]

of Europa within 10 years, and to ice Ih within 20 years [49–55]. A balance between crystallization and amorphization rates will likely result in amorphous water ice forming on the surface with crystalline ice at sub-millimetre depths [48]. However, optical and radar measurements have shown that the grain size of ice on Europa is in the region 25–200 μm [45, 56], that the ice is highly fractured [57], and that the most likely phase of ice at the surface of Europa is Ih [49, 51], which is also the main form of terrestrial sea ice [45]. As the target penetration depth will likely be between 1 and 2 m, the effects of a millimetre or so of amorphous ice on penetration can be ignored. The main chemical contaminants are believed to be sulphuric acid and various salts [58].

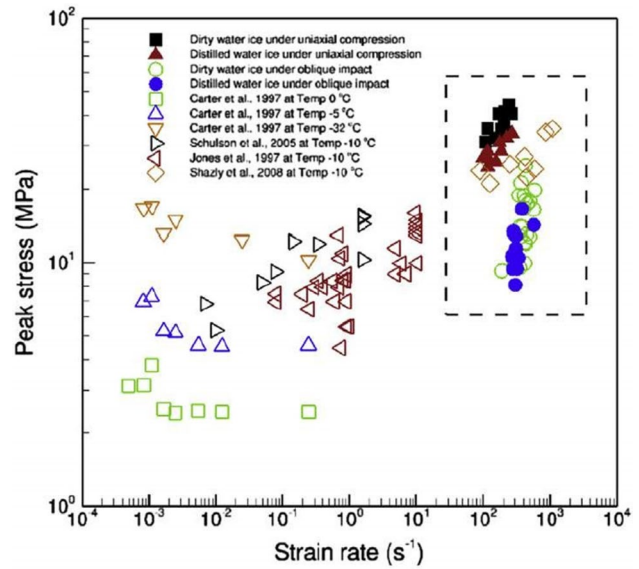


Fig. 3 Plot of peak stress versus strain rate for water ices of various purities loaded in various ways. Figure from [25]. References referred to in the figure: [21, 28, 29] (reference for Carter et al. 1997 omitted from [25])

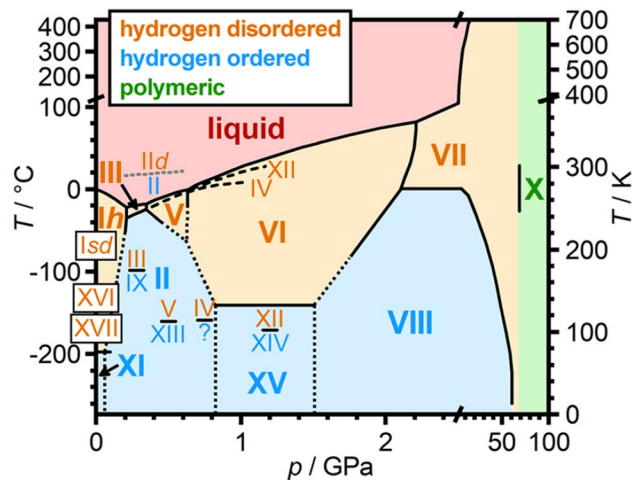


Fig. 4 Recent phase diagram of water ice. From [31]

Specimen Preparation

In order to obtain high-quality mechanical data for ice, care must be taken over specimen preparation. There are three main problems associated with freezing water: (i) ice nucleation takes place preferentially from the surfaces of any container the water is in thereby producing a non-uniform grain structure; (ii) since ice expands on freezing, ice specimens often contain locked-in stresses which can cause spontaneous fracture; (iii) ice is a poorer solvent for air and salts than water resulting in bubbles and brine

inclusions. We therefore decided to expedite the process of specimen manufacture by buying in ice from commercial suppliers who have long experience of making high quality ice for ice sculptures. Such companies make ice using de-ionised water. As a result, the ice they make is clear and free of imperfections (Fig. 5). However, as can also be seen from Fig. 5, they were not able to produce the small specimens (10 mm diameter, 5 mm thick cylinders) that we needed for Hopkinson bar tests. So we had to develop our own low temperature (263 K) machining capability (consisting of a circular saw, a micro lathe and a lapping set-up) so as to be able to make specimens from the larger blocks that Ice Sculptures Ltd. are able to make.

We assessed the porosity of the specimens by (i) measuring their density which we found to be 897.7 kg m^{-3} (literature value 916.7 kg m^{-3}) and (ii) the velocity of ultrasound (measured in two different directions) for a rectangular block of ice of dimensions $110 \text{ mm} \times 110 \text{ mm} \times 200 \text{ mm}$ (Fig. 6). The two values obtained were $3760 \pm 170 \text{ m s}^{-1}$ and $3760 \pm 70 \text{ m s}^{-1}$ (literature values for single crystal ice lie in the range $3700\text{--}4030 \text{ m s}^{-1}$ [59, 60]). The ice can therefore also be assumed to be isotropic.

Experimental

Split Hopkinson Pressure Bar

The high strain rate properties were determined using our split Hopkinson pressure bar (SHPB). The Cavendish SHPB system consists of 12.7 mm diameter, 800 mm long bars made from a number of different materials (Table 1). Acoustic impedance matching is critical for SHPB in order for strong transmission of the loading pulse, as well as allowing the sample to reach force equilibrium faster, providing results that are valid over a wider range of strains. Although our magnesium alloy bars have the closest acoustic impedance to that of ice [61], magnesium's high thermal conductivity would make control of the specimen temperature



Fig. 5 10 mm diameter specimen provided by Ice Sculptures Ltd

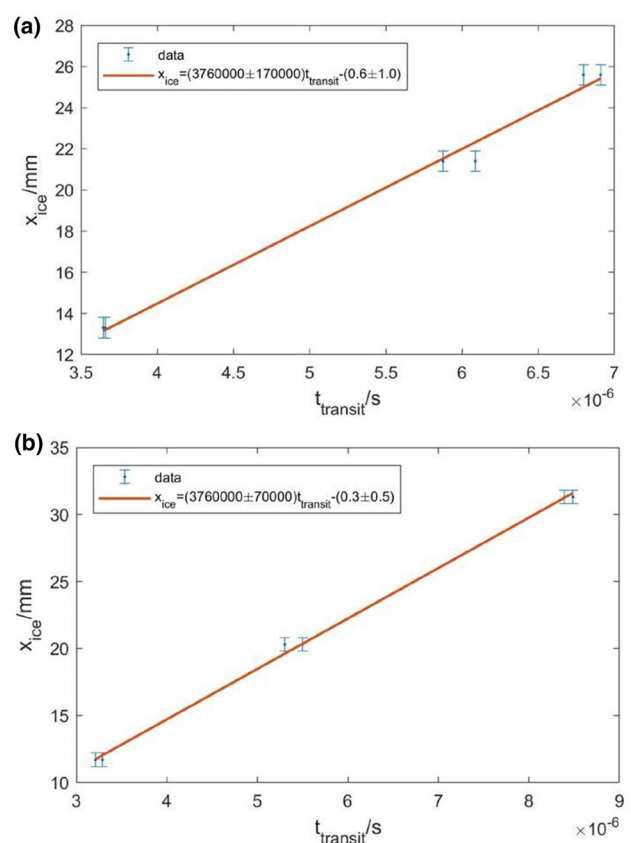


Fig. 6 Plots of distance travelled versus transit time for ultrasound in rectangular blocks of ice of various sizes. **a** Short axis. **b** Long axis

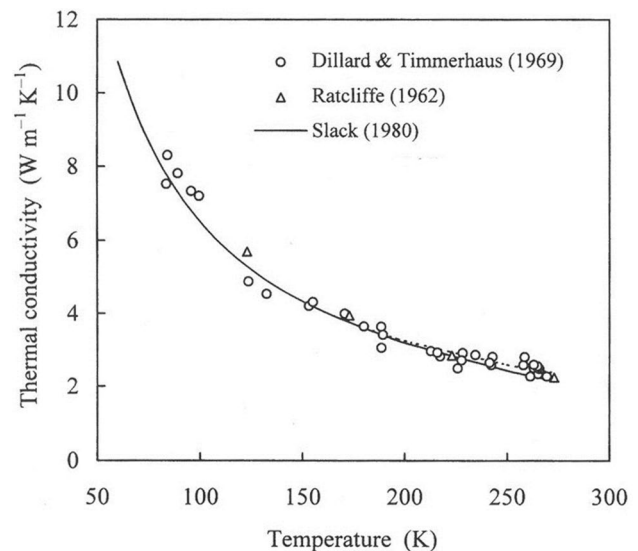


Fig. 7 Plot of the thermal conductivity of pure water ice as a function of temperature. From [62]. Bibliographic information on the publications referred to in the graph: Dillard & Timmerhaus (1969) [63]; Ratcliffe (1962) [64]; Slack (1980) [65]

Table 1 Summary of the acoustic impedances and thermal conductivity of low impedance metal alloys that were considered as Hopkinson bar materials for this study

Material	Impedance/kgm ⁻² s ⁻¹	Thermal conductivity/Wm ⁻¹ K ⁻¹
Ti6Al4 V	21.4 × 10 ⁶	6.7
Dural	13.0 × 10 ⁶	147
Magnesium AZM	8.8 × 10 ⁶	85
Sculpture ice (233 K)	3.4 × 10 ⁶	ca. 3*

The same properties of ice are also given

*Value taken from the graph published in [62] (see also Fig. 7)

problematic. For that reason we decided to use our Ti6Al4 V bars in these experiments.

The bars are instrumented with Kulite AFP 500-90 semiconductor strain gauges that are electrically part of a potential divider held at a constant voltage. Two gauges are mounted in series using a slow-curing epoxy on opposite sides of the bars in order both to double the size of the signal for a given force and also to check for possible bending waves due to impact misalignment. Calibration of the strain gauge/divider system was performed at room temperature according to the procedure described by Siviour [66]. The time-resolution t_{res} of the gauges is given by:

$$t_{\text{res}} = \frac{l_{\text{gauge}}}{c_{\text{bar}}} \quad (1)$$

where l_{gauge} is the length of the gauge (1.5 mm) and c_{bar} is the elastic wave speed in the bar (4840 m/s). Substituting these values in Eq. (1) gives a time resolution of 0.315 μs .

The basic theory of the SHPB has been presented in many publications (e.g. [67–69]), so the derivation of the equations that follow will not be repeated here. The result of an analysis of the interaction of the elastic pulse with the specimen gives the following equations for the engineering stress $s(t)$ and engineering strain rate $\dot{\epsilon}(t)$:

$$s(t) = \frac{F_T(t)}{A_0} \quad (2)$$

$$\dot{\epsilon}(t) = \frac{-2}{l_0 A_b Z_b} F_R(t) \quad (3)$$

where $F_T(t)$ is the force transmitted into the output bar, A_0 is the original cross-sectional area of the specimen, $F_R(t)$ is the force reflected from the specimen back into the input bar, l_0 is the original thickness of the specimen, A_b is the cross-sectional area of the bar, and Z_b is the mechanical impedance of the material the bars are made from. The engineering stress and strain rate can be converted into true stress and

true strain rate assuming the volume of the specimen does not change during deformation [70]. However, since ice is a brittle material we did not perform this conversion as the failure strain was sufficiently small that the values of the two stress and strain measures are the same to well within 1%.

Before performing experiments, the alignment of the bar system was checked to ensure the bars were coaxial. This was done by sending an elastic pulse through the system with no specimen present. The system can be considered aligned when reflection from the input bar-output bar interface is minimal. Good alignment is important when testing a brittle material such as ice as departure from the assumed 1D stress condition could lead to premature fracture.

There are several requirements for classic SHPB theory to hold so as to ensure valid experiments [67–69]:

- The forces on the front and back of the specimen are equal.
- Dispersion of the elastic waves propagating along the rods can be neglected.
- Inertial forces within the specimen are negligible.
- Friction at the specimen/bar interface is negligible.
- Stress waves reflected from the bar ends do not overlap the input and output waves at the position of the strain gauges.
- The stress wave at the bar surface is the same as that within the bar.

These conditions were achieved as follows:

(a) Previous studies showed that it takes from between 3–4 reflections of elastic waves within a specimen to achieve force equilibrium [71–73]. So at least this amount of time must elapse before the stress–strain curves calculated from the recorded strain gauge data can be regarded as accurate. One way of achieving this is to increase the rise time of the loading pulse by placing a piece of copper shim on the impact end of the input bar (Fig. 8) [24, 25, 74–77]. We used colloidal graphite lubricant paste to attach the shim to the bar end.

A check was made on the time taken to reach force equilibrium using the one-wave/two-wave analysis recommended by Gray III [67] when pulse-shaping was used. Force equilibrium was found to occur in the ice specimens after about 10 μs (see Fig. 9). The one-wave analysis uses the force transmitted into the output bar in order to calculate the stress in the specimen, whereas the two-wave analysis uses the sum of the incident and reflected waves to do the calculation. If the results of the two analyses are the same, then force equilibrium has been achieved. To assess this, we used the normalised stress difference $R(t)$ between the two specimen/bar interfaces calculated using:

$$R(t) = \frac{\Delta s(t)}{\bar{s}(t)} \quad (4)$$

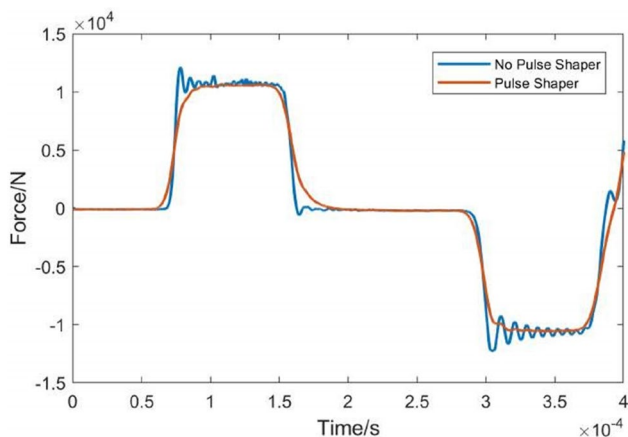


Fig. 8 A comparison between input (loading) pulses with and without pulse shaping

Specimens are taken to be in equilibrium when $R(t) \leq 5\%$. Figure 10 shows that this state occurs between 4–6 wave passes and is achieved more quickly for a ramped pulse than for a top-hat pulse.

(b) Classic SHPB theory assumes the Hopkinson bar behaves as a one-dimensional, nondispersive waveguide [67]. In reality the bars are three-dimensional objects and hence sound waves of different frequencies travel at different speeds [78]. Pulse-shaping the input pulse both increases the rise time (and hence the time to reach peak stress) and reduces the effects of dispersion in the bars (see Fig. 8) [74, 79, 80] thus mitigating the effect of rapid changes in the force applied to the ice specimens (Fig. 9b), something of particular importance for brittle materials [75, 81]. The pieces of copper shim were made slightly larger than the bar diameter so that the copper that had been work-hardened by the punching process used to manufacture them did not participate in the pulse-shaping process (Fig. 11).

(c) During a high rate test, the material of which the specimen is made has to be accelerated from rest. This process generates inertial stresses that add to the measured stress. The fullest derivation of the magnitude of the extra stress on the output end of the specimen is that of Gorham and co-workers [82–84]:

$$\sigma_m - \sigma_a = \rho \left(\frac{h^2}{6} - \frac{a^2}{8} \right) \ddot{\epsilon} + \rho \left(\frac{a^2}{16} - \frac{h^2}{6} \right) \dot{\epsilon}^2 - \frac{\rho h \dot{v}}{2} \quad (5)$$

where σ_m is the measured and σ_a is the actual stress in the sample, h is the specimen thickness, a is the specimen radius, and v is the velocity of the output end of the specimen. An estimate of the error due to inertia for each sample was calculated using Eq. (5). The maximum value was found to be 3.0% (with the majority less than 1%). We therefore

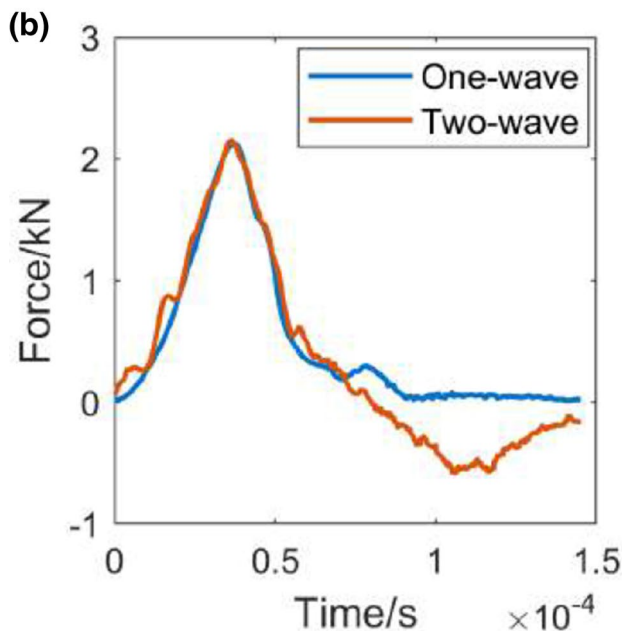
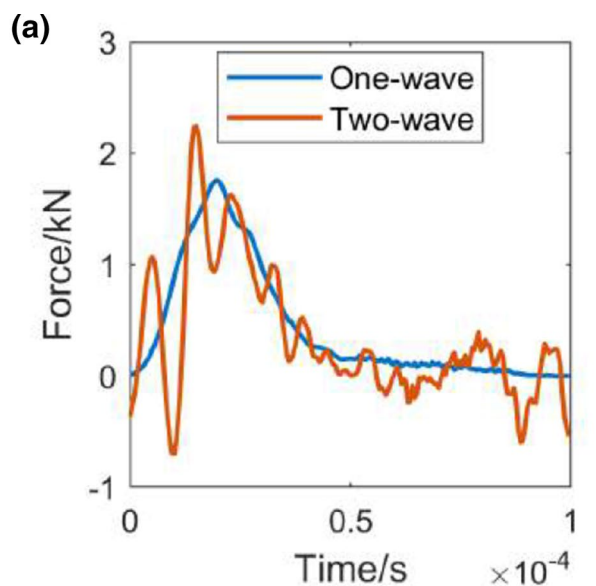


Fig. 9 One-wave and two-wave analyses of data for ice obtained **a** without and **b** with pulse shaping of the input pulse

decided to neglect inertial stresses rather than attempt to correct the results.

(d) An additional source of stress is friction between the surfaces of the specimen and the ends of the bars [71, 84]. Its effect on the measured stress σ_m is given by:

$$\sigma_m = \sigma_{spec} \left(1 + \frac{\mu d}{nl} \right) \quad (6)$$

where σ_{spec} is the stress that would be supported by the specimen in the case of zero friction, μ is the coefficient of friction between the specimen and the bars, d is the specimen

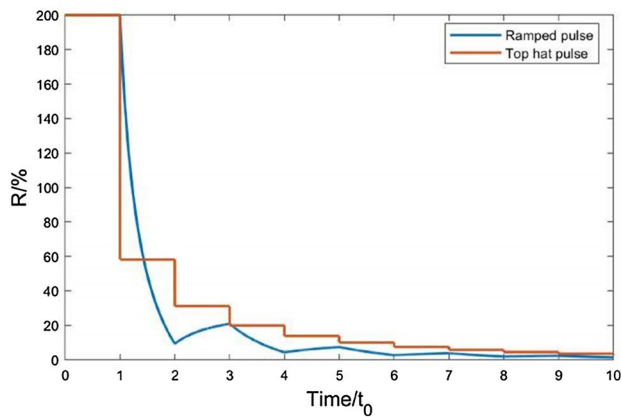


Fig. 10 Comparison of the time to force equilibrium for a ramp-shaped pulse and a ‘top-hat’ pulse

diameter, n is a number whose value depends on the yield criterion for the material being studied, and l is the specimen thickness. Equation (6) shows that there are two possible ways of obtaining σ_{spec} : (i) measure μ under the conditions of the test being used, or (ii) reduce μ to a very low value (ideally zero) using lubrication [84]. Two main ways have been developed for measuring μ in a compression test: (a) perform tests on specimens of different l/d ratios, or (b) perform tests on annular specimens and determine how the ratio of inner to outer diameter develops with time [85]. Both methods would involve making a large number of non-standard specimens. The second (annular) method would also involve using high-speed photography and performing the test between transparent anvils (such as glass) which will almost certainly have a different frictional interaction with the ice. The first method (different aspect ratios) has the disadvantage that although friction has less effect on the measured stress if the cylinder has a large l/d ratio, even ductile materials are more prone to shear failure if this ratio is large [86]. Note that although in everyday life we experience ice as being slippery and hence we think of it as being a low-friction material, this is largely due to the existence of a film of water on the surface which is present either intrinsically or because of heating produced by sliding [87–106]. At the very low temperatures of interest in this study, such a film of water will not be present and so friction must be reduced using lubrication. We found that silicone grease is a suitable lubricant for the temperatures at which these experiments on ice were conducted. This is because it does not alter the mechanical properties of ice and also because the manufacturer claims it maintains its lubricating properties down to 223 K. A previous study showed that no significant difference was observed in the stress–strain response of ice between specimens that were frozen onto the bar and those that were lubricated [21]. However, we found that at 223 K that ‘frozen on’ specimens were significantly stronger than

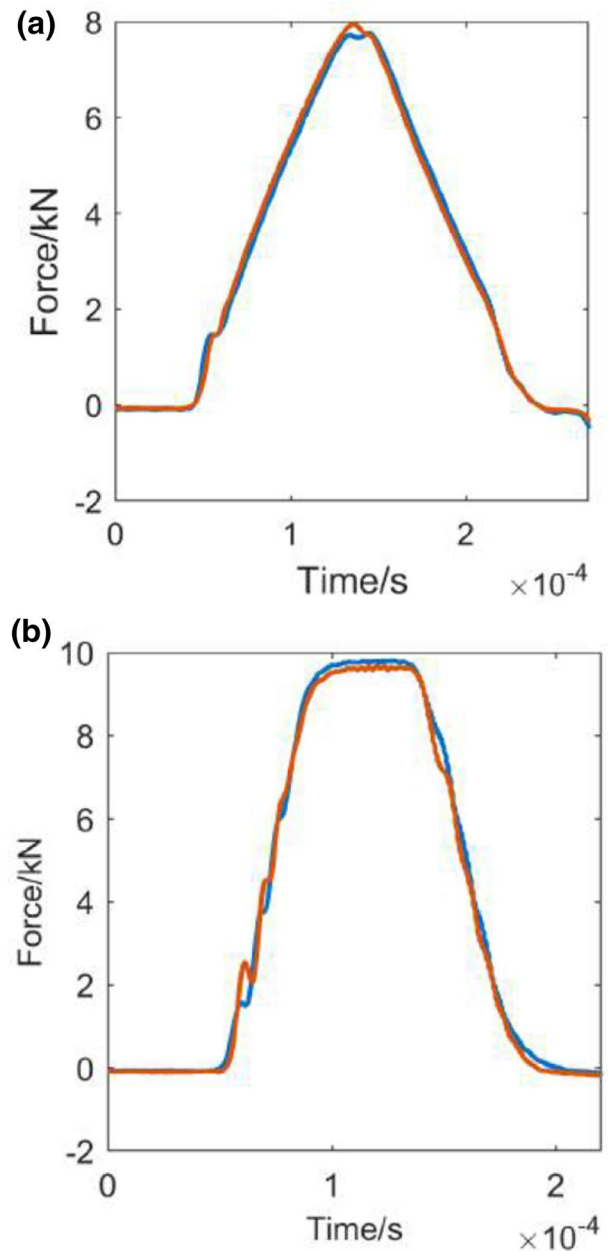


Fig. 11 Plots showing the effect of the dimensions of the copper shim used as a pulse shaper. **a** Thickness 0.61 mm, diameter 3.1 mm. **b** Thickness 0.18 mm, diameter 10.0 mm. Two shots are shown in each graph to demonstrate repeatability

those that were lubricated, perhaps due to the development of a triaxial stress state in the ice. Also tests performed temperatures lower than 198 K showed that the silicone grease exhibited a marked increase in viscosity [107]. Thus tests performed at 173 K and below were lubricated using PTFE dry lubricant spray.

(e) Ensuring overlap between the forward and backward travelling elastic waves does not occur within the SHPB can be achieved by careful attention to the lengths of the various

bars in the system. The temporal duration of the incident pulse is equal to two wave transit times in the striker bar. In practice the input pulse has a longer duration than this due to dispersion. So if the striker and input bars are made of the same material, wave overlap can be avoided if the striker is less than half the length of the input bar. Since in our system the input and output bars used are approximately 800 mm long and the striker bar used was 144 mm long, the required condition is satisfied.

(f) Uniformity of the stress within the elastic pulses at the position of the strain gauges occurs because St. Venant's principle (which states that the details of the load distribution on the loading surface do not matter as long as the stress is measured sufficiently far from that surface) can be extended to dynamic loading [108, 109]. Gorham et al. found that the strain gauges should be at least 10 bar diameters from the end of the bars [83]. This condition was more than satisfied for the 12.7 mm diameter bars used in this investigation by attaching the strain gauges 250 mm away from the specimen position.

Temperature

The ends of the SHPB bars were enclosed in an environmental chamber that was kept cold using dry nitrogen gas that was cooled by passing it through a coiled copper pipe immersed in liquid nitrogen. The chamber is made from Teflon and has a sliding fit to the bars so as to ensure containment of the cold nitrogen gas, while at the same time putting minimal lateral mechanical constraint on the bars. The temperature of the environmental chamber was monitored using thermocouples and this information was used to control the power output of an in-line heating element (Omega gas heater, part number AHP-7562) so that the temperature of the nitrogen flowing into the chamber remained constant and at the value required for a given experiment (see Fig. 12).

As shown in Table 1, Ti6Al4 V bars were chosen for this study because of their low thermal conductivity. However, thermal contraction and thermal gradients are also an issue.

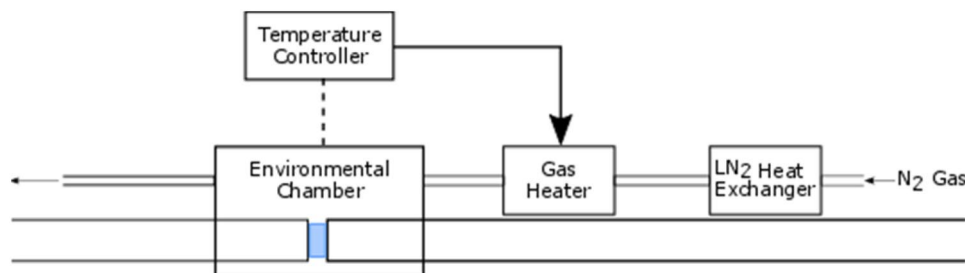


Fig. 12 Schematic diagram of the temperature control system used to regulate the temperature in an environmental chamber enclosing the ends of our SHPB used for obtaining mechanical data at high rates

Thermal contraction was allowed for by making the holes in the ends of the environmental chamber of a diameter such that the cold gas within the chamber will still satisfactorily be contained down to a temperature of 173 K. Concerning thermal gradients, Kishida et al. showed that their effect on the mechanical impedance of steel rods (and hence on elastic pulse propagation) can be neglected in the temperature range 4–570 K [110].

We performed a simple experiment to see whether this was true for our bar system. The experiments consisted of placing the end of the Ti6Al4 V input bar inside the environmental chamber kept at 175 K. Figure 13 compares a pulse so obtained with one where the whole bar was at ambient temperature (295 K), the striker velocities being the same to within 0.4%. As the height of the incident pulses are the same we may conclude that the responses of the gauges are unaffected by cooling the end of the bars. The temperature at the gauges during the cold test was measured as being 292 K, which is within the range of ambient temperatures in the laboratory.

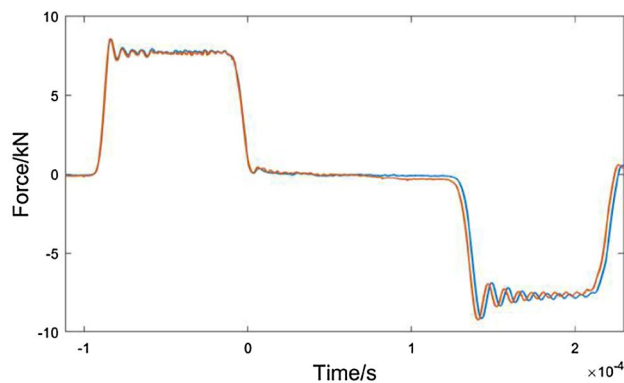


Fig. 13 A plot comparing a stress pulse in the input bar (measured using strain gauges at a temperature of 292 K) when one end of the bar was cooled to 175 K (orange line) with a stress pulse in the input bar when the whole bar was at 295 K (blue line). The velocity of the striker bar was 5.49 m/s for the 295 K experiment and 5.51 m/s for the 175 K test (Color figure online)

of strain. The same system was also used to enclose the anvils in an Instron mechanical testing machine for low strain rate tests

One noticeable difference between the pulses is that there is some decrease in transit time of the pulse in the cooled bar. This is because the stiffness of a material, and thus the sound speed, depends on temperature. A change in stiffness could also cause distortion of the strain pulse near the specimen or even some reflection of elastic wave energy. However, no reflection of elastic waves from the cold section was observed, suggesting that cooling a section of the bars will not affect the experimental results. The potential dividers have also been designed such that the system is robust to temperature changes at the gauges [66].

The above checks having been made, we were confident that the data obtained from the strain gauges could be analysed using standard SHPB analysis [67].

Ice Specimens

As may be seen from Fig. 14, the grain size of the ice is comparable to the size of the specimens. In order to achieve consistency in the data, as far as possible only single crystal samples were used. However, the crystallographic orientation of the cylindrical specimens was not determined. One possible way of doing this without using X-rays would be

to measure the through-thickness sound speeds of both longitudinal and transverse waves since their values depend on the angle of the direction of measurement with the c -axis (Fig. 15).

Another problem in conducting these experiments is the thermal expansion and contraction of the ice as the

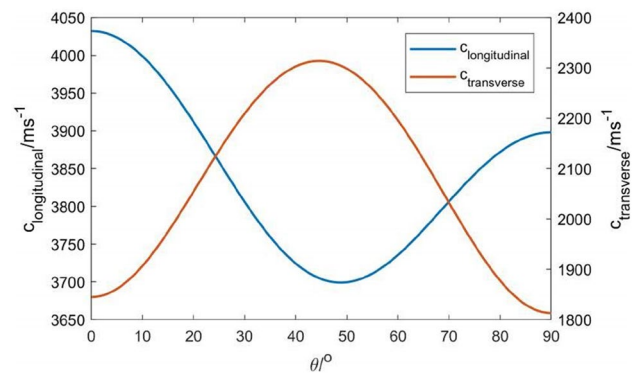
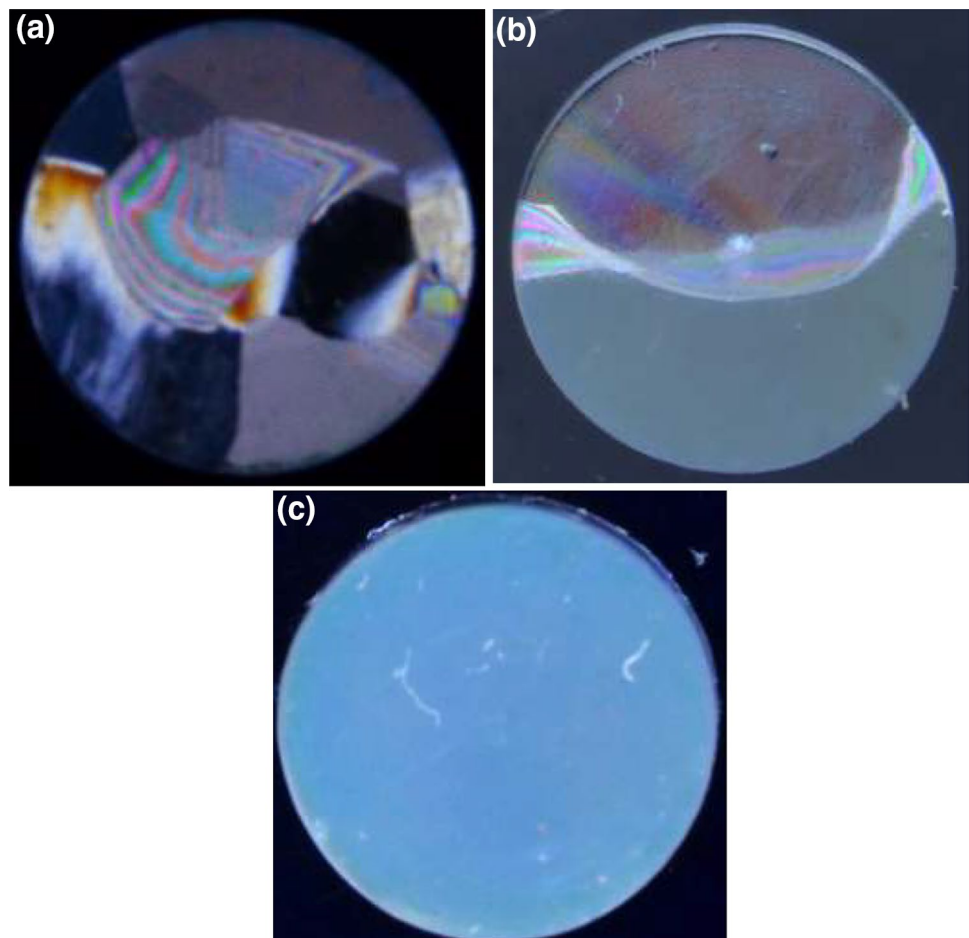


Fig. 15 Plot of the dependence of the longitudinal and transverse (shear) sound speeds for ice as a function of angle between the direction of measurement and the c -axis. Data obtained from [59, 111]

Fig. 14 Cross-polar photographs of some of our 10 mm diameter, 5 mm thick ice cylinders. **a** Polycrystalline specimen formed by lapping and turning. **b** Two-crystal specimen formed by turning only. **c** Single-crystal specimen formed by turning only



temperature is changed. The dimensions of the specimens were measured at 258 K using a micrometer but were then tested at greater or lower temperatures. The calculated percentage change in length as the temperature is lowered from 263 to 173 K can be seen in Fig. 16. This graph was generated using published values for the ice unit cell volumes at different temperatures [112]. The length change can be significant being, for example, $-0.417 \pm 0.027\%$ at 173 K. Thermal expansion/contraction was incorporated into the analysis as we found that failure occurred at strains of around 1%.

Another problem caused by length change in the specimens when the temperature is reduced is loss of contact with one of the bars. The loss of contact can be observed in the experimental results by the apparent attainment of large strains under little to no stress (Fig. 17). A more serious problem is that until the specimen is in contact with both bars, the end of the input bar is a free surface so that the incoming input wave will be reflected and the specimen will initially not be loaded by a ramped loading pulse. This could cause early failure for the reasons discussed earlier. It is therefore important that the bars are pushed together just before testing to ensure good sample-bar contact.

Low Rate Testing

The compressive strengths of ice at low strain rates were measured using an Instron mechanical testing machine. A large quantity of low rate data exists for ice, so performing low-rate experiments makes possible a comparison of our ice

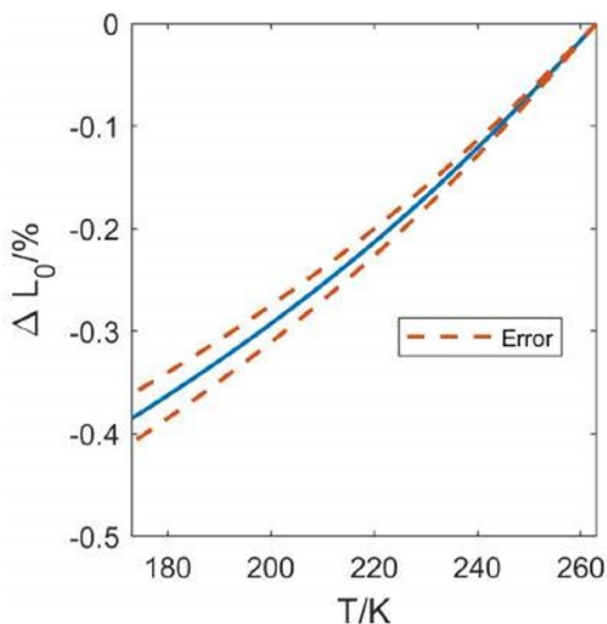


Fig. 16 The percentage length change of a specimen initially measured at 263 K as the temperature is lowered to 173 K

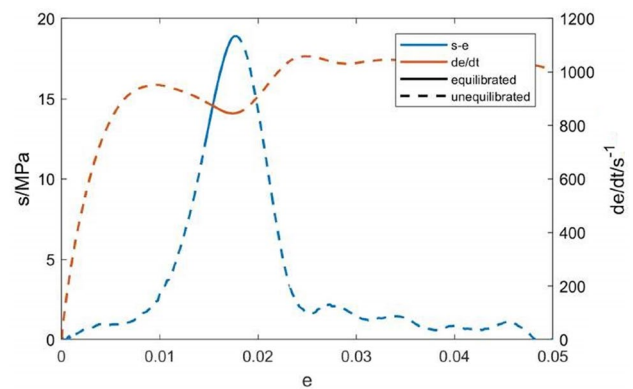


Fig. 17 An example of a calculated stress–strain curve for ice in which contact with one of the bars had been lost before the test due to thermal contraction

with those reported in the literature. Low-rate experiments are also needed for a full constitutive description such as Johnson-Holmquist, one of the best devised so far for brittle materials [113–115].

Photographs of the experimental set-up are shown in Fig. 18. The force was applied to the specimen through a rod connected to the load-cell located in the cross-head. Silicone grease was used as a lubricant between the anvils and the ice. The separation of the anvils was directly measured using clip-gauges. The gauges were calibrated at room temperature and then connected to the anvils before cooling to eliminate any offset from thermal contraction.

Since ice is a brittle material, care was taken to ensure that the anvils were both flat and parallel to each other so as to avoid non-uniform loading which is known to produce premature failure [116]. Alignment and parallelism was ensured using epoxy resin to glue the anvils in place while under compression.

For cryogenic testing, the same temperature control system was used as in the SHPB tests. As can be seen in Fig. 18, an expanded polystyrene box was placed around the anvils to form an environmental chamber. The anvils were also thermally isolated from the Instron machine using Macor (a machinable glass–ceramic obtainable from Corning). The temperatures of the anvils and gas were measured using thermocouples and an average value was calculated. The specimen dimensions were the same as those used in the SHPB tests. The time required for the ice specimens to thermally equilibrate was calculated by simulation.

Results

Figure 19 presents all the data we obtained for the engineering peak stress s_{peak} supported by ice at three different strain rates within the range 10^{-3} to 10^{+3} s^{-1} and at temperatures

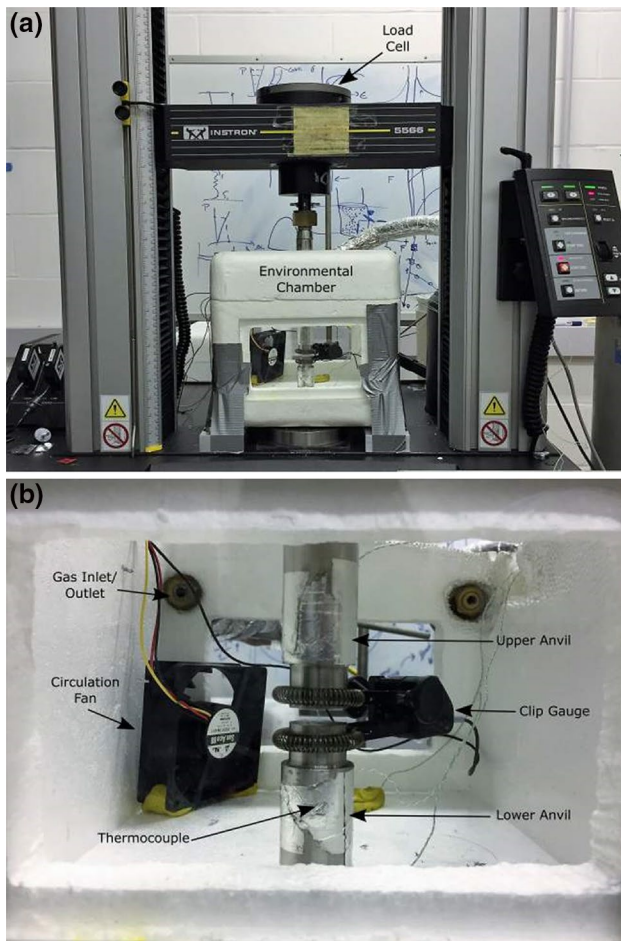


Fig. 18 The experimental set-up for low rate testing. The Instron has been modified for low-temperature testing using by placing an environmental chamber around the anvils. The load cell measures the force through the anvils. Clip gauges can be seen attached to the anvils in order to measure their separation

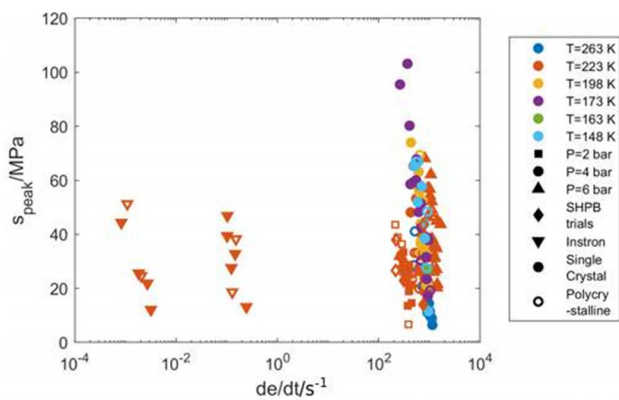


Fig. 19 Plot of the peak stress obtained quasistatically and at Hopkinson bar rates of strain for ice at various ambient temperatures

ranging from 148 to 263 K. As mentioned earlier in this article, engineering stress s and strain e were used since ice, being a brittle material, can only support a small strain (the difference between true and engineering strains is negligible for small deformations [70]).

Figure 20 presents typical engineering stress–strain and engineering strain-rate curves for ice tested in our SHPB at 223 K. The initial dotted line indicates where the specimen was not in stress equilibrium. The ice then undergoes a roughly linear-elastic rise until the peak stress s_{peak} and failure strain e_{fail} are reached. The peak stress at this temperature lay in the range 38 ± 18 MPa and the failure strain in the range 0.012 ± 0.005 .

Conclusions and Suggestions for Future Research

Techniques have been developed for preparing small cylindrical specimens (10 mm diameter, 5 mm thick) from blocks of pure water–ice supplied by a commercial company. These specimens were used to obtain data on the low rate (10^{-3} and 10^{-1} s^{-1}) and high rate (10^{+3} s^{-1}) compressive stress–strain response of single crystal ice at temperatures in the range 148 to 263 K. The data obtained will be used to parameterise the Johnson-Holmquist constitutive model for ice and this will be reported in more detail in a future paper. The ice at the surface of Europa is likely to be weaker than pure ice at a given temperature. These techniques and the resulting data are vital in derisking any future penetrator missions to Europa by improving the simulation capability of the impact.

In order to perform these tests, a temperature control system and environmental chambers were developed for our split Hopkinson pressure bar (SHPB) and Instron mechanical testing machines. Copper shim was used to

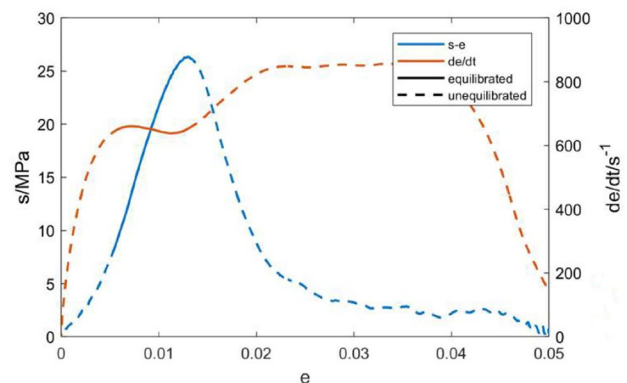


Fig. 20 Plot showing a typical engineering stress–strain curve (blue line) and the corresponding engineering strain rate (orange line) for ice tested at 223 K in our SHPB. The solid line indicates the section of the curves where the specimen was intact and in stress equilibrium (Color figure online)

ramp the loading pulses in our SHPB so as to reduce the rate at which the strain-rate applied to our brittle ice specimens increased.

The Instron tests showed no difference between the peak engineering stresses at strain rates in the range 10^{-3} to 10^{-1} s^{-1} , the average value for s_{peak} across all experiments being $35 \pm 19 \text{ MPa}$. It was also observed that the strength of ice increased as the temperature was reduced from 263 to 173 K. For the whole set of SHPB experiments (230 to 1660 s^{-1}), the average engineering peak stress was found to be $38 \pm 18 \text{ MPa}$.

Lubrication with silicone grease was shown to reduce the measured peak stress, but silicone grease only works as a lubricant down to around 173 K. Powdered PTFE was used at temperatures lower than this.

The results indicate that there is no significant difference in strength between polycrystalline and single crystal specimens. However, the crystal orientation was not determined. At quasistatic rates the strength of single crystal ice has been found to depend on orientation [117]. So it is recommended that future SHPB studies should aim to account for the microstructure of ice specimens, through the development of an ice growth capability and the use of an automatic fabric analyzer.

Also in any future tests the effect of specimen-bar contact should be carefully accounted for. Furthermore, the systematic differences between the peak stresses obtained by specimens loaded using pulses of different magnitudes should be investigated further. It would also be interesting to utilize the results obtained in the current work for simulation development.

To further de-risk a possible penetrator mission, studies at lower temperatures on briny and damaged ices should be undertaken in order to study conditions more representative of Europa.

In conclusion, the results presented in this paper should be of interest to computational groups looking to model ice impact as it will allow for the parameterisation of some of the more common constitutive models that are available. However, care should be taken to include a statistical failure or yield criterion that can account for some of the variation in the data available, particularly if the model is of a small-scale system. Additionally, if models are being made from a more fundamental bottom up approach in order to replicate experimental data, care should be taken around parameters such as grain shape and orientation as well as interfacial friction.

Acknowledgements Gratitude is expressed to David Page-Croft of the Department of Applied Mathematics and Theoretical Physics, University of Cambridge for his assistance during the use of their cold room for sample preparation. We also thank QinetiQ plc for funding through the IRAD programme.

Open Access This article is distributed under the terms of the Creative Commons Attribution 4.0 International License (<http://creativecommons.org/licenses/by/4.0/>), which permits unrestricted use, distribution, and reproduction in any medium, provided you give appropriate credit to the original author(s) and the source, provide a link to the Creative Commons license, and indicate if changes were made.

References

- Weiss P, Yung KL, Kömle N, Ko SM, Kaufmann E, Kargl G (2011) Thermal drill sampling system onboard high-velocity impactors for exploring the subsurfaces of Europa. *Adv Space Res* 48:743–754
- Wurz P, Lasi D, Thomas N, Piazza D, Galli A, Jutzi M, Barabash S, Wieser M, Magnes W, Lammer H, Auster U, Gurvits LI, Hajdas W (2017) An impacting descent probe for Europa and the other Galilean moons of Jupiter. *Earth Moon Planets* 120:113–146
- Winglee RM, Robinson T, Danner M, Koch J (2018) Cryobraking using penetrators for enhanced capabilities for the potential landing of payloads on icy solar system objects. *Acta Astronaut* 144:136–146
- White C, Scanlon TJ, Merrifield JA, Kontis K, Langener T, Alves J (2016) Numerical and experimental capabilities for studying rocket plume-regolith interactions. *AIP Conf Proc* 1786:170003
- Stewart ST, Ahrens TJ (2003) Shock Hugoniot of H_2O ice. *Geophys Res Lett.* <https://doi.org/10.1029/2002gl016789>
- Stewart ST, Ahrens TJ (2005) Shock properties of H_2O ice. *J Geophys Res* 110:E03005
- Stewart ST, Seifert A, Obst AW (2008) Shocked water ice: thermal emission measurements and the criteria for phase changes during impact events. *Geophys Res Lett* 35:L23203
- Kraus RG, Stewart ST, Seifert A, Obst AW (2010) Shock and post-shock temperatures in an ice-quartz mixture: implications for melting during planetary impact events. *Earth Planet Sci Lett* 289:162–170
- Kraus RG, Senft LE, Stewart ST (2011) Impacts onto H_2O ice: scaling laws for melting, vaporization, excavation, and final crater size. *Icarus* 214:724–738
- Senft LE, Stewart ST (2011) Modeling the morphological diversity of impact craters on icy satellites. *Icarus* 214:67–81
- Orlov MY, Orlova Y, Bogomolov G, Glazyrin V (2017) Research of the behavior of ice on water under explosive loads. *J Phys: Conf Ser* 919:012006
- Ross B (1969) Perforation of Arctic sea-ice cover by projectile impact. *J Hydronautics* 3:115–120
- Ross B, Hanagud S, Sidhu G (1971). Penetration studies of ice with application to arctic and subarctic warfare. Naval Ordnance Laboratory, Silver Spring, MD, Report no. AD0736633
- Young CW (1974) Penetration of sea ice by air-dropped projectiles. *Proc IEEE International Conference on Engineering in the ocean environment*, vol 1. IEEE, New York, pp 89–95
- Aitken GW, Swinzow GK, Farrell DR (1976) Projectile and fragment penetration in snow and frozen soil. US Army Cold Regions Research and Engineering Laboratory, Hanover
- Aitken GW (1978). Terminal ballistics in cold regions materials. In: *Proc 4th Int Symp on Ballistics*. Arlington VA: American Defence Preparedness Association. Session 6, paper 6
- Lange MA, Ahrens TJ (1982) Fragmentation of ice by low velocity impact. *Proc 12th Lunar and Planetary Science Conf*. Pergamon, Oxford, pp 1667–1687
- Young CW (1997). Penetration equations. Sandia National Laboratory, Albuquerque, NM, Report no. SAND97-2426

19. Carney KS, Benson DJ, DuBois P, Lee R (2006) A phenomenological high strain rate model with failure for ice. *Int J Solids Structures* 43:7820–7839
20. Kim H, Keune JN (2007) Compressive strength of ice at impact strain rates. *J Mater Sci* 42:2802–2806
21. Shazly M, Prakash V, Lerch BA (2009) High strain rate behavior of ice under uniaxial compression. *Int J Solids Structures* 46:1499–1515
22. Combescure A, Chuzel-Marmot Y, Fabis J (2011) Experimental study of high-velocity impact and fracture of ice. *Int J Solids Structures* 48:2779–2790
23. Bragov A, Igumnov L, Konstantinov A, Lomunov A, Filippov A, Shmotin Y, Didenko R, Krundaeva A (2015) Investigation of strength properties of freshwater ice. *EPJ Web Conf* 94:01070
24. Wu XQ, Prakash V (2015) Dynamic compressive behavior of ice at cryogenic temperatures. *Cold Regions Sci Technol* 118:1–13
25. Wu XQ, Prakash V (2015) Dynamic strength of distilled water and lake water ice at high strain rates. *Int J Impact Eng* 76:155–165
26. Church P, Lewtas I, Gould P, Braithwaite C, Jardine A (2016) Development and validation of high strain rate model for water ice. In: Woodley C, Cullis I (eds) *Proc 29th Int Symp on Ballistics*. Lancaster, PA, DesTech, pp 1977–1988
27. Schulson EM (2001) Brittle failure of ice. *Engng Fract Mech* 68:1839–1887
28. Schulson EM, Iiescu D, Fortt A (2005). Characterization of ice for return-to-flight of the Space Shuttle. 1: Hard ice. National Aeronautics and Space Administration, Washington DC, Report no. CR-2005-213643/Part 1
29. Jones SJ (1997) High strain-rate compression tests on ice. *J Phys Chem B* 101:6099–6101
30. Cheng BQ, Engel EA, Behler J, Dellago C, Ceriotti M (2019) Ab initio thermodynamics of liquid and solid water. *Proc Nat Acad Sci USA* 116:1110–1115
31. Salzmann CG (2019) Advances in the experimental exploration of water's phase diagram. *J Chem Phys* 150:060901
32. Medjani K (1996) Numerical simulation of the formation of brine pockets during the freezing of the NaCl-H₂O compound from above. *Int Commun Heat Mass Transfer* 23:917–928
33. Wells AJ, Wettlaufer JS, Orszag SA (2011) Brine fluxes from growing sea ice. *Geophys Res Lett* 38:L04501
34. Wei PS, Huang CC, Lee KW (2003) Nucleation of bubbles on a solidification front: experiment and analysis. *Metall Mater Trans B* 34:321–332
35. Yoshimura K, Inada T, Koyama S (2008) Growth of spherical and cylindrical oxygen bubbles at an ice-water interface. *Cryst Growth Design* 8:2108–2115
36. Hooke RL, Dahlin BB, Kauper MT (1972) Creep of ice containing dispersed fine sand. *J Glaciol* 11:327–336
37. Park JH, Lee JS (2014) Characteristics of elastic waves in sand-silt mixtures due to freezing. *Cold Regions Sci Technol* 99:1–11
38. Gundlach B, Schmidt KP, Kreuzig C, Bischoff D, Rezaei F, Kothe S, Blum J, Grzesik B, Stoll E (2018) The tensile strength of ice and dust aggregates and its dependence on particle properties. *Mon Not Royal Astron Soc* 479:1273–1277
39. Moslet PO (2007) Field testing of uniaxial compression strength of columnar sea ice. *Cold Regions Sci Technol* 48:1–14
40. Timco GW, Weeks WF (2010) A review of the engineering properties of sea ice. *Cold Regions Sci Technol* 60:107–129
41. Li ZJ, Zhang LM, Lu P, Leppäranta M (2011) Experimental study on the effect of porosity on the uniaxial compressive strength of sea ice in Bohai Sea. *Sci China Technol Sci* 54:2429–2436
42. Goldstein RV, Osipenko NM (2015) Some aspects of strength in sea ice mechanics. *Phys Mesomech* 18:139–148
43. Han HW, Li ZJ, Huang WF, Lu P, Lei RB (2015) The uniaxial compressive strength of the Arctic summer sea ice. *Acta Ocean Sinica* 34:129–136
44. Fink UWE, Larson HP (1975) Temperature dependence of water-ice spectrum between 1 and 4 microns: application to Europa, Ganymede, and Saturn's rings. *Icarus* 24:411–420
45. Ligier N, Poulet F, Carter J, Brunetto R, Gorgeot F (2016) VLT/SINFONI observations of Europa: new insights into the surface composition. *Astron J* 151(6):163
46. Hall DT, Strobel DF, Feldman PD, McGrath MA, Weaver HA (1995) Detection of an oxygen atmosphere on Jupiter moon Europa. *Nature* 373:677–679
47. Mateo-Marti E, Prieto-Ballesteros O, Sobrado JM, Gomez-Elvira J, Martin-Gago JA (2006) A chamber for studying planetary environments and its applications to astrobiology. *Meas Sci Technol* 17:2274–2280
48. Carlson RW, Calvin WM, Dalton JB (2009) Europa's surface composition. In: Pappalardo RT, McKinnon WB, Khurana KK (eds) *Europa*. University of Arizona Press, Tucson, pp 283–327
49. Kouchi A, Yamamoto T, Kozasa T, Kuroda T, Greenberg JM (1994) Conditions for condensation and preservation of amorphous ice and crystallinity of astrophysical ices. *Astron Astrophys* 290:1009–1018
50. Baragiola RA (2003) Water ice on outer Solar System surfaces: basic properties and radiation effects. *Planet Space Sci* 51:953–961
51. Hansen GB, McCord TB (2004) Amorphous and crystalline ice on the Galilean satellites: a balance between thermal and radiolytic processes. *J Geophys Res* 109:E01012
52. Famá M, Loeffler MJ, Raut U, Shi J (2008) Radiation effects in ice: new results. *Nuclear Instrum Meth Phys Res B* 266:3057–3062
53. Zheng WJ, Jewitt D, Kaiser RI (2009) On the state of water ice on Saturn's moon Titan and implications to icy studies in the outer solar system. *J Phys Chem A* 113:11174–11181
54. Famá M, Loeffler MJ, Raut U, Baragiola RA (2010) Radiation-induced amorphization of crystalline ice. *Icarus* 207:314–319
55. Rothard H, Domaracka A, Boduch P, Palumbo ME, Strazzulla G, da Silveira EF, Dartois E (2017) Modification of ices by cosmic rays and solar wind. *J Phys B* 50:062001
56. Dalton JB, Shirley JH, Kamp LW (2012) Europa's icy bright plains and dark linea: exogenic and endogenic contributions to composition and surface properties. *J Geophys Res* 117:E03003
57. Moore JM, Black G, Buratti R, Phillips CB, Spencer J, Sullivan R (2009) Surface properties, regolith, and landscape degradation. In: Pappalardo RT, McKinnon WB, Khurana KK, Dotson R (eds) *Europa*. University of Arizona Press, Tucson, pp 329–349
58. Fischer PD, Brown ME, Hand KP (2015) Spatially-resolved spectroscopy of Europa: the distinct spectrum of large-scale chaos. *Astron J* 150(5):164
59. Gammon PH, Kieft H, Clouter MJ (1983) Elastic constants of ice samples by Brillouin spectroscopy. *J Phys Chem* 87:4025–4029
60. Gammon PH, Kieft H, Clouter MJ, Denner WW (1983) Elastic constants of artificial and natural ice samples by Brillouin spectroscopy. *J Glaciology* 29:433–460
61. Gagnon RE, Kieft H, Clouter MJ, Whalley E (1990) Acoustic velocities and densities of polycrystalline ice Ih, ice II, ice III, ice V, and ice VI by Brillouin spectroscopy. *J Chem Phys* 92:1909–1914
62. Petrenko VF, Whitworth RW (1999) Thermal properties of ice. *Physics of ice*. Oxford University Press, Oxford, pp 40–45
63. Dillard DS, Timmerhaus KD (1969) Low temperature thermal conductivity of selected dielectric crystalline solids. In: Ho CY,

- Taylor RE (eds) Proc Eighth Conf on thermal conductivity. Plenum, New York, pp 949–967
64. Ratcliffe EH (1962) The thermal conductivity of ice: new data on the temperature coefficient. *Philos Mag* 7:1197–1203
 65. Slack GA (1980) Thermal conductivity of ice. *Phys Rev B* 22:3065–3071
 66. Siviour CR (2005). High strain rate properties of materials using Hopkinson bar techniques. PhD thesis, Univ. of Cambridge
 67. Gray GT III (2000) Classic split-Hopkinson pressure bar testing. In: Kuhn H, Medlin D (eds) *ASM Handbook Vol 8: mechanical testing and evaluation*. Materials Park, OH, ASM International, pp 462–476
 68. Chen W, Song B (2011) *Split Hopkinson (Kolsky) Bar: design, testing and applications*. Springer, New York
 69. Othman R (ed) (2018) *The Kolsky-Hopkinson Bar Machine: Selected Topics*. Springer, Berlin
 70. Johnson W, Mellor PB (1973) *Engineering plasticity*. van Nostrand Reinhold, London, p 4
 71. Davies EDH, Hunter SC (1963) The dynamic compression testing of solids by the method of the split Hopkinson pressure bar. *J Mech Phys Solids* 11:155–179
 72. Briscoe BJ, Nosker RW (1984) The influence of interfacial friction on the deformation of high density polyethylene in a split Hopkinson pressure bar. *Wear* 95:241–262
 73. Ravichandran G, Subhash G (1994) Critical appraisal of limiting strain rates for compression testing of ceramics in a split Hopkinson pressure bar. *J Am Ceram Soc* 77:263–267
 74. Nemat-Nasser S, Isaacs JB, Starrett JE (1991) Hopkinson techniques for dynamic recovery experiments. *Proc R Soc Lond A* 435:371–391
 75. Frew DJ, Forrestal MJ, Chen W (2002) Pulse shaping techniques for testing brittle materials with a split Hopkinson pressure bar. *Exper Mech* 42:93–106
 76. Chen XD, Ge LM, Zhou JK, Wu SX (2016) Experimental study on split Hopkinson pressure bar pulse-shaping techniques for concrete. *ASCE J Mater Civil Eng* 28:04015196
 77. Song ZH, Wang ZH, Kim H, Ma HW (2016) Pulse shaper and dynamic compressive property investigation on ice using a large-sized modified split Hopkinson pressure bar. *Latin Am J Solids Struct* 13:391–406
 78. Davies RM (1948) A critical study of the Hopkinson pressure bar. *Phil Trans Roy Soc London A* 240:375–457
 79. Parry DJ, Walker AG, Dixon PR (1995) Hopkinson bar pulse smoothing. *Meas Sci Technol* 6:443–446
 80. Ramesh KT (2008) High rates and impact experiments. In: Sharpe WN (ed) *Springer handbook of experimental solid mechanics*. Springer, Berlin, pp 929–960
 81. Subhash G, Ravichandran G (2000) Split-Hopkinson bar testing of ceramics. In: Kuhn H, Medlin D (eds) *ASM Handbook Vol 8: mechanical testing and evaluation*. Materials Park, OH, ASM International, pp 497–504
 82. Gorham DA (1989) Specimen inertia in high strain-rate compression. *J Phys D Appl Phys* 22:1888–1893
 83. Gorham DA, Pope PH, Field JE (1992) An improved method for compressive stress-strain measurements at very high strain rates. *Proc R Soc London A* 438:153–170
 84. Siviour CR, Walley SM (2018) Inertial and frictional effects in dynamic compression testing. In: Othman R (ed) *The Kolsky-Hopkinson bar machine*. Springer, Berlin, pp 205–247
 85. Walley SM, Field JE, Pope PH, Safford NA (1989) A study of the rapid deformation behaviour of a range of polymers. *Phil Trans R Soc London A* 328:1–33
 86. Radford DD, Walley SM, Church P, Field JE (2003) Dynamic upsetting and failure of metal cylinders: experiments and analysis. *J Phys IV France* 110:263–268
 87. Faraday M (1850) On certain conditions of freezing water. *J Franklin Inst* 50:283–284
 88. Person CC (1850) Sur la chaleur latente de fusion de la glace. *CR Acad Sci Paris* 30:526–528
 89. Person CC (1851) Latent heat of water. *J Franklin Inst* 51:189–190
 90. Forbes JD (1858) On some properties of ice near its melting point. *J Franklin Inst* 66:402–404
 91. Faraday M (1860) Note on regelation. *Proc R Soc London* 10:440–450
 92. Bowden FP, Hughes TP (1939) The mechanism of sliding on ice and snow. *Proc R Soc London A* 172:280–298
 93. Bowden FP (1953) Friction on snow and ice. *Proc R Soc London A* 217:462–478
 94. Nakaya U, Matsumoto A (1954) Simple experiment showing the existence of liquid water film on the ice surface. *J Colloid Sci* 9:41–49
 95. Ambach W, Mayr B (1981) Ski gliding and water film. *Cold Regions Sci Technol* 5:59–65
 96. Maruyama M, Satoi T, Taniguchi S, Kawamura M, Kadera S, Kishimoto Y, Furukawa Y (2000) X-ray analysis of the structure of premelted layers at ice interfaces. *Jpn J Appl Phys* 39:6696–6699
 97. Sadtchenko V, Ewing GE (2002) Interfacial melting of thin ice films: an infrared study. *J Chem Phys* 116:4686–4697
 98. Liu SH, Luo JB, Li G, Zhang CH, Lu XC (2008) Effect of surface physicochemical properties on the lubricating properties of water film. *Appl Surf Sci* 254:7137–7142
 99. Thomson ES, Hansen-Gooe H, Wettlaufer JS, Wilen LA (2013) Grain boundary melting in ice. *J Chem Phys* 138:124707
 100. Murata K, Asakawa H, Nagashima K, Furukawa Y, Sazaki G (2016) Thermodynamic origin of surface melting on ice crystals. *Proc Nat Acad Sci USA* 113:E6741–E6748
 101. Matveev KI (2017) An analytical model for flat-ski friction in steady horizontal gliding. *Sports Eng* 20:293–298
 102. Bokarev VP, Krasnikov GY (2018) Model of coordination melting of crystals and anisotropy of physical and chemical properties of the surface. *Surf Sci* 668:73–79
 103. Ovaska M, Tuononen AJ (2018) Multiscale imaging of wear tracks in ice skate friction. *Tribol Int* 121:280–286
 104. Qiu YQ, Molinero V (2018) Why is it so difficult to identify the onset of ice premelting? *J Phys Chem Lett* 9:5179–5182
 105. Scherge M, Böttcher R, Spagni A, Marchetto D (2018) High-speed measurements of steel-ice friction: experiment vs. calculation. *Lubricants* 6(1):26
 106. Sugimoto T, Otsuki Y, Ishiyama T, Morita A, Watanabe K, Matsumoto Y (2019) Topologically disordered mesophase at the topmost surface layer of crystalline ice between 120 and 200 K. *Phys Rev B* 99:121402
 107. Bair S, Casalini R (2008) A scaling parameter and function for the accurate correlation of viscosity with temperature and pressure across eight orders of magnitude of viscosity. *Trans ASME* 130:041802
 108. Kennedy LW, Jones OE (1969) Longitudinal wave propagation in a circular bar loaded suddenly by a radially distributed end stress. *Trans ASME* 36:470–478
 109. Safford NA (1992) Materials testing up to 10^5 s^{-1} using a miniaturised Hopkinson bar, with dispersion corrections. In: Zhang G, Huang S (eds) *Proc 2nd Int Symp on intense dynamic loading and its effects*. Sichuan University Press, Chengdu, pp 378–383
 110. Kishida K, Kataoka T, Yokoyama T, Nakano M (1987) Behaviour of materials at high strain rates and cryogenic temperature. In: Kawata K, Shioiri J (eds) *Macro- and micro-mechanics of high velocity deformation and Fracture*. Springer-verlag, Berlin, pp 75–84

111. Gammon PH, Kiefte K, Clouter MJ, Denner WW (1981) Note on analysis of acoustic data from hexagonal monocrystals of unknown orientation. *J Acoust Soc Am* 69:1503–1504
112. Rottger K, Endriss A, Ihringer J, Doyle S, Kuhs WF (1994) Lattice constants and thermal expansion of H₂O and D₂O ice Ih between 10 and 265K. *Acta Cryst B* 50:644–648
113. Holmquist TJ, Johnson GR (2011) A computational constitutive model for glass subjected to large strains, high strain rates and high pressures. *Trans ASME* 78:051003
114. Holmquist TJ, Johnson GR, Gerlach CA (2017) An improved computational constitutive model for glass. *Phil Trans R Soc A* 375:20160182
115. Walley SM (2014) An introduction to the properties of silica glass in ballistic applications. *Strain* 50:470–500
116. Kuhn HA (2000) Uniaxial compression testing. In: Kuhn H, Medlin D (eds) *ASM handbook Vol 8: mechanical testing and evaluation*. Materials Park, OH, ASM International, pp 143–151
117. Trickett YL, Baker I, Pradhan PMS (2000) The orientation dependence of the strength of ice single crystals. *J Glaciology* 46:41–44

Publisher's Note Springer Nature remains neutral with regard to jurisdictional claims in published maps and institutional affiliations.